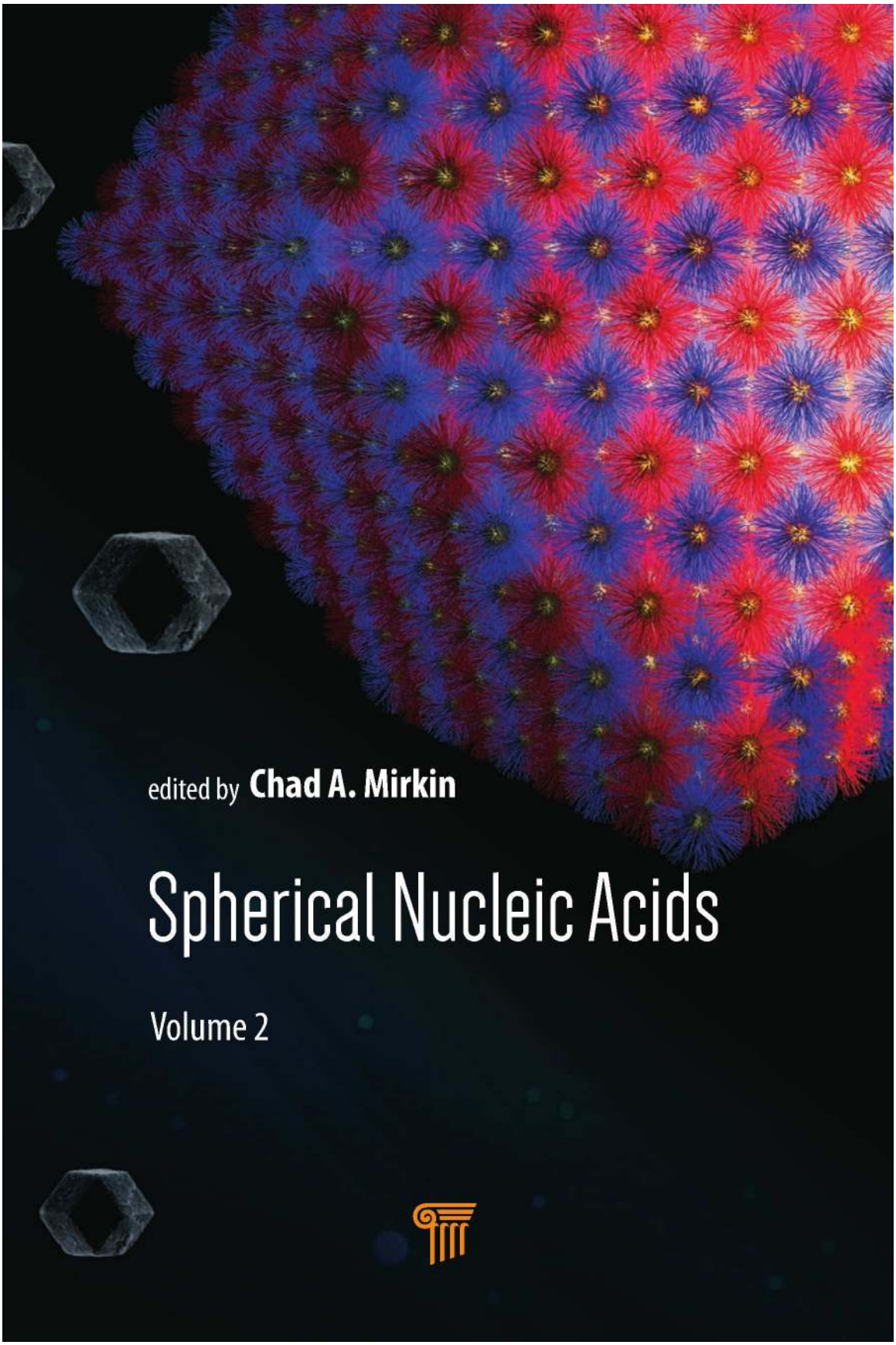
edited by Chad A. Mirkin
Spherical Nucleic Acids
Volume 2

Taylor & Francis
Taylor & Francis Group
http://taylorandfrancis.com

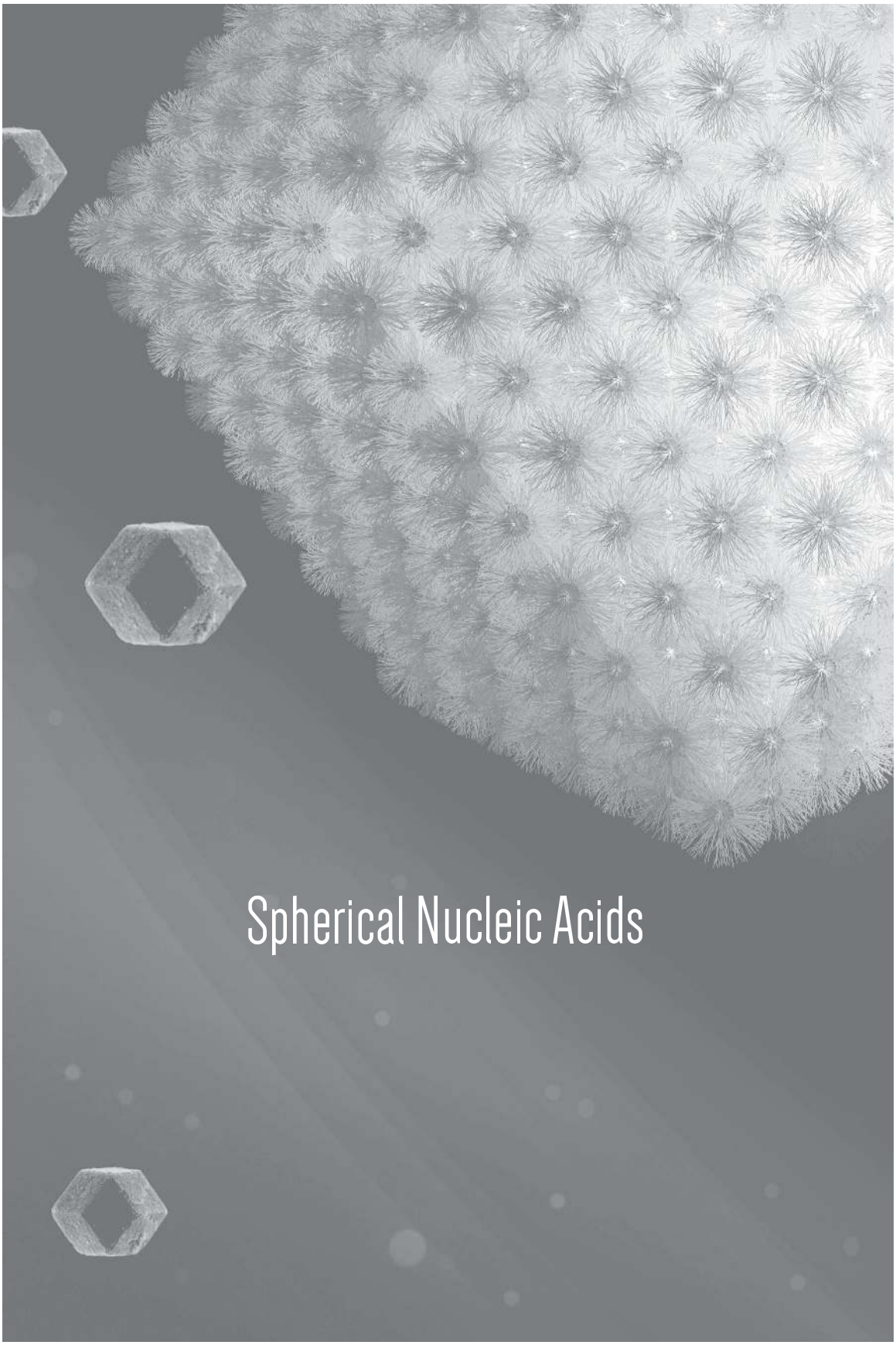
Spherical Nucleic Acids

Taylor & Francis
Taylor & Francis Group
http://taylorandfrancis.com

Spherical Nucleic Acids

Volume 2

edited by

Chad A. Mirkin

JENNY STANFORD
PUBLISHING

Published by

Jenny Stanford Publishing Pte. Ltd.
Level 34, Centennial Tower
3 Temasek Avenue
Singapore 039190

Email: editorial@jennystanford.com
Web: www.jennystanford.com

British Library Cataloguing-in-Publication Data
A catalogue record for this book is available from the British Library.

Spherical Nucleic Acids, Volume 2

ISBN 978-981-4800-35-8 (Set) (Hardcover)
ISBN 978-0-429-20015-1 (Set) (eBook)
ISBN 978-981-4877-22-0 (Volume 2) (Hardcover)
ISBN 978-1-003-05669-0 (Volume 2) (eBook)

Contents

Chapter 46

Electrolyte-Mediated Assembly of Charged Nanoparticles*

Sumit Kewalramani,[a] Guillermo I. Guerrero-García,[a,b] Liane M. Moreau,[a] Jos W. Zwanikken,[a] Chad A. Mirkin,[a,c] Monica Olvera de la Cruz,[a,c,d] and Michael J. Bedzyk[a,d]

[a]*Department of Materials Science and Engineering, Northwestern University, 2220 Campus Drive, Evanston, IL 60208, USA*

[b]*Instituto de Física, Universidad Autonoma de San Luis Potosí, Alvaro Obregon 64, 78000 San Luis Potosí, San Luis Potosí, Mexico*

[c]*Department of Chemistry, Northwestern University, 2145 Sheridan Road, Evanston, IL 60208, USA*

[d]*Physics and Astronomy Department, Northwestern University, 2145 Sheridan Road, Evanston, IL 60208, USA*

m-olvera@northwestern.edu; bedzyk@northwestern.edu

Solutions at high salt concentrations are used to crystallize or segregate charged colloids, including proteins and polyelectrolytes

*Reprinted with permission from Kewalramani, S., Guerrero-García, G. I., Moreau, L. M., Zwanikken, J. W., Mirkin, C. A., Olvera de la Cruz, M. and Bedzyk, M. J. (2016). Electrolyte-mediated assembly of charged nanoparticles, *ACS Cent. Sci.* **2**, 219–224. <https://pubs.acs.org/doi/10.1021/acscentsci.6b00023>. Further permissions related to the material excerpted should be directed to the ACS.

Spherical Nucleic Acids, Volume 2
Edited by Chad A. Mirkin

ISBN 978-981-4877-22-0 (Hardcover), 978-1-003-05669-0 (eBook)
www.jennystanford.com

via a complex mechanism referred to as "salting-out." Here, we combine small-angle X-ray scattering (SAXS), molecular dynamics (MD) simulations, and liquid-state theory to show that salting-out is a long-range interaction, which is controlled by electrolyte concentration and colloid charge density. As a model system, we analyze Au nanoparticles coated with noncomplementary DNA designed to prevent interparticle assembly via Watson–Crick hybridization. SAXS shows that these highly charged nanoparticles undergo "gas" to face-centered cubic (FCC) to "glass-like" transitions with increasing NaCl or $CaCl_2$ concentration. MD simulations reveal that the crystallization is concomitant with interparticle interactions changing from purely repulsive to a "long-range potential well" condition. Liquid-state theory explains this attraction as a sum of cohesive and depletion forces that originate from the interelectrolyte ion and electrolyte–ion–nanoparticle positional correlations. Our work provides fundamental insights into the effect of ionic correlations in the salting-out mechanism and suggests new routes for the crystallization of colloids and proteins using concentrated salts.

46.1 Introduction

Controlling the crystallization of colloids, including proteins, from solutions has been a scientific goal for decades [1–7]. The crystallization of charged colloids is often induced by using high salt concentrations, a process referred to as "salting-out" [7]. Colloids can also be concentrated and crystallized via the well-understood depletion forces induced by the addition of polymers [5, 8] or micelle forming surfactants [9]. However, colloidal crystallization in high ionic strength solutions is subtle and not understood. Crystallization via "salting-out" is observed for specific salts in a narrow range of salt concentrations, when the interparticle interactions are weakly attractive [10]. Above this salt concentration range, in the regime of stronger attractive interactions, amorphous precipitates are observed. It is generally believed that short-ranged attractions due to ionic correlations and solvation effects drive the colloidal assembly [11]. By contrast, the present study reveals that, in high ionic strength solutions, the interparticle attraction between like-

charged nanoparticles extends a few nm from the colloidal surface. This "long-range" attraction is induced by the electrolyte ions, and is not an effect of van der Waals forces.

Long-range interactions between like-charged colloids near surfaces [12, 13] have been explored for decades. These interactions are attractive near surfaces due to hydrodynamic effects [14], but in bulk solutions they are found to be purely repulsive [15]. Here, we show that electrolyte-mediated long-range interparticle attractions are possible in bulk solutions in the regime of high ionic strength. To enhance the electrostatic coupling between the nanoparticles and the electrolyte ions, our experimental design used highly charged (>2000 e^-/nanoparticle) DNA coated spherical gold nanoparticles (AuNPs) in solutions containing high concentrations of NaCl or $CaCl_2$. To avoid interparticle assembly via Watson–Crick hybridization [16, 17], we used DNAs that lacked self-complementary single-stranded sticky ends. Naively, one might expect that, in the absence of hybridization, the interactions between DNA coated AuNPs are purely repulsive. Here, small-angle X-ray scattering (SAXS) shows that, depending on the salt concentration and the DNA, FCC crystals are formed with nearest-neighbor distances (d_{NN}) that are comparable with twice the nanoparticle hydrodynamic radius R. This demonstrates the emergence of concentrated electrolyte-mediated attractions.

Various mean field theories have been developed to compute the effective interactions between charged colloids, for example, the Derjaguin–Landau–Verwey–Overbeek (DLVO) [18] theory and its extensions that include the renormalized charges of the colloids. However, at high ionic strengths these models cannot account for the correlations among ions surrounding strongly charged colloids. Recently, numerical techniques have elucidated that ionic correlations in confined concentrated electrolytes can induce attractions between like-charged surfaces at concentrations larger than 300 mM NaCl [19]. These attractions are distinct from the multivalent ($Z \geq 3$) counterion-mediated attractions in DNA and other polyelectrolytes [20–22], which are observed at low ionic strengths (μM– mM), are short-ranged (a few Å corresponding to the multivalent ion diameter), and lead to unstable precipitates in the absence of specific short-range attractions as the salt concentration increases. Here, we find attractions at high ionic strengths (>100 mM) and even in monovalent salts, resembling the "salting-out" effect.

By molecular dynamics (MD) simulations and liquid-state theory we provide evidence that the ionic correlations in the concentrated electrolyte induce interparticle long-range attractions and drive the assembly.

46.2 Results and Discussion

46.2.1 SAXS Studies of DNA-Coated AuNP Assembly

To analyze the effect of charge density, DNA rigidity, and electrolyte concentration, we studied four sample sets. These sets correspond to two nanoparticle types: AuNPs (nominally, 10 nm diameter) functionalized with single-stranded (ss)-DNA (ssDNA-AuNP) or double-stranded (ds)-DNA (dsDNA-AuNP) (insets, Figs. 46.1A and C), each dispersed in two solution types, NaCl and $CaCl_2$. For all samples, the nanoparticle concentration was ~50 nM, corresponding to an average center-to-center interparticle distance of ~400 nm in the gas phase. For each set, ionic strengths (μ_s) in the range ~30–2000 mM were examined. By definition, for NaCl solutions, μ_s = [NaCl] and for $CaCl_2$ solutions, $\mu_s = 3 \times [CaCl_2]$. In salt-free solutions, dynamic light scattering (DLS) yield hydrodynamic radii of $R \approx 19$ nm and $R \approx 13$ nm for ssDNA-AuNP and dsDNA-AuNP, respectively, corresponding to volume fractions of $\sim 8.7 \times 10^{-4}$ and $\sim 2.7 \times 10^{-4}$. These salt-free values mark the upper bounds for the volume fractions since the radial extension of the DNA on the nanoparticles, as expected [23], is found to decrease with increasing μ_s due to the enhanced screening of the intra-DNA electrostatic repulsions.

For all the sample sets, Fig. 46.1 shows representative SAXS intensity profiles (I) as a function of the scattering vector magnitude q ($= 4\pi \sin\theta/\lambda$). Here, λ is the X-ray wavelength and 2θ is the scattering angle. For ssDNA-AuNPs in NaCl solutions, the main features of the intensity profiles are μ_s-independent. To illustrate, two extreme μ_s cases are shown in Fig. 46.1A. These SAXS profiles exhibit the characteristics of scattering from isolated DNA-coated-AuNPs, which is predominantly due to the electron-dense Au cores [24]. Based on SAXS from a solid homogeneous sphere [25], the position of the first minima ($q_{min} \approx 1$ nm^{-1}) corresponds to a Au core radius of $R_{Au} = \sim 4.5/q_{min} = 4.5$ nm. Unlike ssDNA-AuNPs in NaCl

solutions, ssDNA-AuNPs in $CaCl_2$ or dsDNA-AuNPs in NaCl or $CaCl_2$ solutions aggregate into clusters above a threshold ionic strength μ_t, as evidenced by the appearance of sharp intensity modulations in the $q < 1$ nm^{-1} region (Fig. 46.1B–D). DLS measurements show that a typical cluster size is ~1.7 μm.

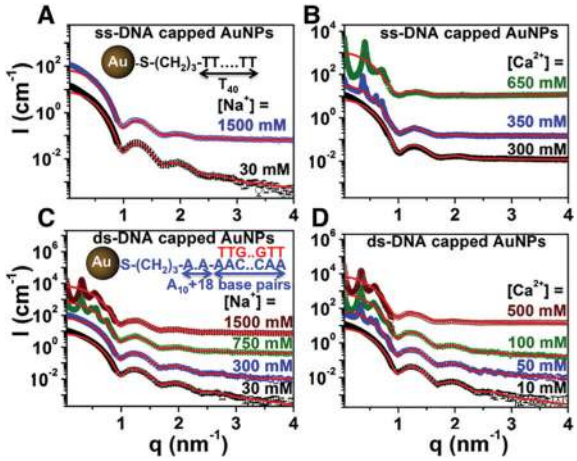

Figure 46.1 Ionic-strength-dependent assembly behavior of DNA coated AuNPs. 1D SAXS intensity profiles for ssDNA-AuNP and dsDNA-AuNP in NaCl (A, C) and $CaCl_2$ (B, D) solutions. The data shown is the scattered intensity above the background scattering from empty capillary and pure water. The insets in panels A and C show the DNA-grafted-AuNP components. There are ~60 thiolated-DNA tethered to each AuNP. About 40% of the strands on dsDNA-AuNPs were in duplexed form. The ssDNA is a T_{40} strand. The DNA chain in panel C consists of a 10 base long ssDNA spacer A_{10} and an 18 base-pair long dsDNA segment. Therefore, the total charge on the nanoparticles is ~2400 e^-/NP and ~2100 e^-/NP for ssDNA-AuNP and dsDNA-AuNP, respectively. Solid red lines are the expected scattered intensities from isolated DNA-grafted-AuNPs.

Comparison of μ_t in different sample sets shows that Ca^{2+} induces aggregation of DNA-coated-AuNPs at much lower μ_s than Na^+ (Figs. 46.1C and D). Similarly, dsDNA-AuNPs form aggregates at a much lower μ_s than ssDNA-AuNPs (Figs. 46.1B and D). Thus, the DNA-coated-AuNPs form aggregates more readily when the DNA charge density and the counterion valency are increased. These trends indicate that the responsible attractions cannot originate from van der Waals forces.

Figure 46.1 shows the simulated intensities $P(q)$ for isolated DNA-grafted-AuNPs (solid red lines). For all the cases where nanoparticle aggregation is not observed, the measured $I(q)$ are well described by simulations based on mean Au core size $\langle R_{Au} \rangle$ = 4.5 nm and polydispersity (PD) = 8.5% or $\langle R_{Au} \rangle$ = 4.4 nm and PD = 7.7%, depending upon the nanoparticle batch used. This analysis allows extraction of the structure factor [$S(q) = I(q)/P(q)$] for nanoparticle aggregates (Figs. 46.2A and B).

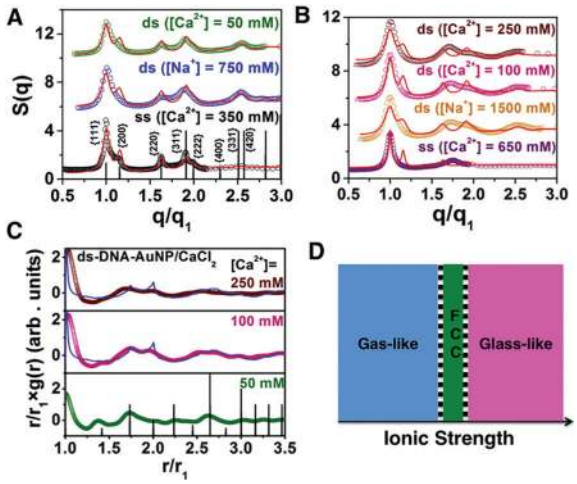

Figure 46.2 Structure of DNA coated AuNP assemblies. (A, B) SAXS-derived $S(q)$ for DNA-grafted-AuNP aggregates (circles) along with simulations based on FCC lattices (red lines). For reference, the expected peak positions and relative intensities for Bragg reflections from ideal FCC lattices are shown (A, vertical black lines). The labels ss and ds correspond to ssDNA-AuNP and dsDNA-AuNP, respectively. (C) Representative radial distribution functions for dsDNA-AuNPs in $CaCl_2$ as a function of μ_s along with the expected positions and relative populations ($P/12$) for neighbors in a FCC lattice (black lines). For visual comparisons, $g(r)$ is plotted against normalized radial distance r/r_1. Here, $r_1 = d_{NN}$ represents the nearest-neighbor interparticle distance. Monte Carlo simulations for $g(r)$ based on random close packing (RCP) of hard spheres (blue lines) reasonably describe the experimental $g(r)$ for μ_s much higher than μ_t. (D) Schematic of the observed changes in colloidal packing as a function of ionic strength.

Two types of $S(q)$ profiles are observed. First, regardless of the DNA-coating and the salt solution, $S(q)$ exhibits similar features at the threshold ionic strength (μ_t) for aggregation. These $S(q)$ are

plotted against q/q_1 (Fig. 46.2A), where, q_1 is the position of the principal peak. Similarly, for $\mu_s >> \mu_t$, $S(q)$ vs. q/q_1 profiles are nearly identical (Fig. 46.2B), but subtly different from the profiles at $\mu_s = \mu_t$. The analysis of $S(q)$ based on a formalism by Förster et al. [26] shows that, for $\mu_s = \mu_t$, DNA functionalized AuNPs are arranged on FCC lattices (Fig. 46.2A). The positions of the principal FCC (1 1 1) peak yield lattice parameters $a_{FCC}\left(=\frac{\sqrt{12}\pi}{q_1}\right)$ = 29.2, 36.7, and 34.4 nm for ssDNA-AuNPs in $CaCl_2$, and dsDNA-AuNPs in NaCl and $CaCl_2$ solutions, respectively. For the three cases in Fig. 46.2A, the widths of the (h k l) diffraction profiles yield average crystallite sizes of 200–300 nm. Taken together, the DLS-measured aggregate size (1.7 μm) and the SAXS-derived crystallite size imply that the DNA-grafted-AuNPs assemble into polycrystalline aggregates at ionic strengths equal to or slightly above μ_t. Therefore, under appropriate conditions, electrolyte-mediated interactions can induce crystalline order in DNA functionalized AuNPs even in the absence of Watson–Crick hybridization.

Figure 46.2B shows that, for $\mu_s >> \mu_t$, the assembly does not consist of FCC crystallites. More information about the nanoparticle packing in these aggregates is gleaned from radial distribution function $g(r)$. Figure 46.2C shows the μ_s-dependence of $g(r)$ for dsDNA-AuNPs in $CaCl_2$ solutions. For the 50 mM [Ca^{2+}] case ($\mu_s = \mu_t$), the amplitudes and the positions of maxima in $g(r)$ at r/r_1 = 1, $\sqrt{2}$, $\sqrt{3}$, $\sqrt{4}$, $\sqrt{5}$, etc. are consistent with FCC lattices (Fig. 46.2C, bottom). With increasing μ_s, the $r/r_1 = \sqrt{2}$ modulation smears out. Further, the $g(r)$ exhibit a slightly split doublet with nearly equal amplitude maxima at $r/r_1 \approx \sqrt{3}$ and $\approx \sqrt{4}$ (Fig. 46.2C, middle and top). This doublet is a signature of a glassy phase [27]. Specifically, the $g(r)$ for [Ca^{2+}] = 100 mM (Fig. 46.2C, middle) resembles the $g(r)$ for the "metallic-glass-like" packing of spherical colloids [2]. Similarly, the $g(r)$ for [Ca^{2+}] = 250 mM, where the $r/r_1 = \sqrt{2}$ feature is mostly smeared out, is reminiscent of the $g(r)$ for random-close-packed (RCP) spheres [28]. These observations imply that the packing of DNA-grafted-AuNPs transforms from isolated particles (gas-like) to face centered cubic (FCC) to "glass-like" arrangement with increasing μ_s (Fig. 46.2D). The structural phase transition sequence is similar to that observed for protein crystallization [10]. Furthermore, similar to the case of

proteins, the crystallization of DNA-coated AuNPs occurs in a narrow μ_s regime, for example, $\mu_s \approx 1050-1500$ mM for ssDNA-AuNP in $CaCl_2$. Our results suggest that the electrolyte concentration induced "gas" to "crystalline" to "amorphous" transitions are a general feature of the assembly of charged colloids in high-ionic-strength solutions.

Some insight into the assembly mechanism of DNA-grafted-AuNPs is obtained from the (nearest-neighbor distance) d_{NN} versus μ_s trends. First, the d_{NN} continuously decreases with increasing μ_s to reach a constant value in the glassy state, which is ~94% of the d_{NN} observed for FCC crystals at $\mu_s = \mu_t$. Second, the observed d_{NN} are smaller than estimates for $2R$ that are based on the combination of modified Daoud–Cotton model parameters [23] for the ssDNA radial extension and the experimental values for the average inter-base-pair separation for dsDNA in Watson–Crick hybridization-driven assemblies [29]. Both these observations suggest a dense packing of DNA-grafted-AuNPs that is driven by electrolyte-mediated attractions.

46.2.2 MD Simulations for Potential of Mean Force between DNA-Coated AuNPs

The hypothesis of electrolyte-mediated interparticle attractions was validated by MD simulations. Figure 46.3A shows the potential of mean force between two dsDNA-AuNPs as a function of the distance between their centers in the presence of an electrolyte with divalent cations and monovalent anions (2:1 electrolyte). Here, the two DNA-grafted-AuNPs interact only via short-ranged repulsive steric interactions, and long-ranged Coulomb potentials. Two values of μ_s were simulated: 15 mM ($\mu_s << \mu_t$) and 150 mM ($\mu_s = \mu_t$). For the 15 mM case, the interaction is repulsive for all interparticle separations. At the onset of crystallization (150 mM case), the potential barrier at low interparticle separations reflects the steric and electrostatic repulsions arising due to the strong interdigitation of the DNA strands on neighboring nanoparticles. However, the effective potential is clearly attractive over a ~7 nm wide region. The minima position in the interparticle potential (Fig. 46.3A) corresponds to the case where the DNA coronas of the two nanoparticles are just touching (Fig. 46.3B). Thus, the interparticle interactions are attractive at separation distances

where dsDNA chains with maximum extension can overlap slightly, but also at separation distances that are ~4 nm larger than the tangential contact distance between the nanoparticles (Fig. 46.3C). The range of attractive interactions is approximately *five times higher* than the Debye screening length (κ^{-1} = 0.78 nm) for μ_s = 150 mM. Attractions between high charge density macromolecules such as DNA in bulk solutions [30] and at interfaces [31] have been previously observed at or above μ_s = 150 mM for 2:1 electrolytes. However, these attractions were hypothesized to be short-ranged, with a decay length comparable to the hydrated divalent cation diameter.

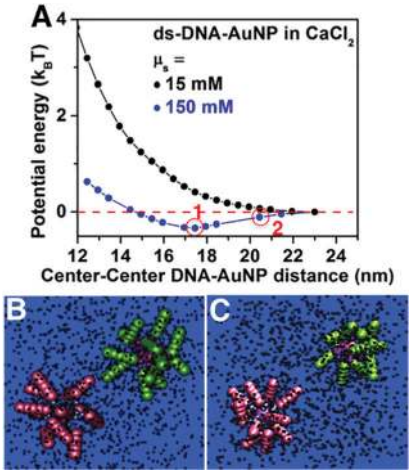

Figure 46.3 Effective interaction potential between two DNA-grafted-AuNPs. (A) Potential energy as a function of interparticle separation for two dsDNA-AuNPs in two solutions of different μ_s. The minima position (circled point 1) corresponds to tangential contact between the two dsDNA capped AuNPs. Simulation snapshots corresponding to circled points 1 and 2 are shown in panels B and C, respectively.

Due to computational constraints, the MD simulations were performed for R_{Au} = 1.5 nm particles with 12 DNA/AuNP and only for 2:1 electrolytes at the two ionic strengths described above. Correcting for the radius of the AuNPs, MD simulations show that the equilibrium inter-dsDNA-AuNP separation is 23.6 nm, close to the experimental $d_{NN} = (a\text{FCC}/\sqrt{2})$ = 24.3 nm for the μ_s = 150 mM case. The nanoparticle size-correction should also be applied to the

potential well depth ($\sim 0.33 k_B T$, Fig. 46.3A). This is because liquid-state theory (next section) shows that the magnitude of the two-body attraction depends on the nanoparticle size. The size-corrected potential well depth is $0.45 k_B T$.

The interparticle attractive potential well is shallow. However, crystallization is a many-particle collective process. Taking into account only the coordination number of 12 in a FCC lattice, the potential energy/particle becomes $\sim 5.4 k_B T$. Considerations of DNA-coated nanoparticles at finite concentration could further increase this energy estimate via inclusion of multiparticle effects that are absent in our potential of mean force calculations, due to the assumption of infinite dilution of nanoparticles. We note that the attractive potential well condition coincides with a strong enhancement in the cation–anion positional correlations in the supporting electrolyte and the DNA corona.

Finally, previous simulation studies that utilized simplifying assumptions of screened Coulomb or Yukawa-like effective potentials [32] yielded short-ranged attractions between functionalized nanoparticles. Now, by explicitly considering the positional correlations between electrolyte ions in bulk solutions and between the electrolyte ions and the nanoparticles, our simulations reveal the long-range nature of the observed electrolyte mediated attractions.

46.2.3 Liquid-State Theory for Like-Charged Attraction

Insights into the origin of the attraction between like-charged objects are provided by a liquid-state-theory based analytical approach. Specifically, the interaction potential between the nanoparticles can be derived from first principles in an algebraic form that distinguishes contributions from ion entropy and ion–nanoparticle and interion correlations. The range of the interaction is connected to the length over which the nanoparticles influence the ionic density profile in the electrolyte. This length typically extends beyond the radial size of the DNA linkers because of electrostatic and steric interactions [24]. At low salt concentrations, this extension is well approximated by the Debye length, whereas at high concentrations, it is typically larger than the Debye length, measuring a few hydrated ionic radii.

To illustrate like-charge attraction in a simpler case, we calculate the potential of mean force between like-charged ions in primitive electrolytes. Figure 46.4A shows that, at sufficiently high concentrations, like charges attract, mediated by opposite charges. These attractions appear roughly above 0.1 M for a 1:1 electrolyte of the primitive model (e.g., NaCl) and a few tens of mM for 2:1 electrolyte (e.g., $CaCl_2$). Furthermore, the range of the interaction is greater than 2.5 nm (6–7 × the hydrated ionic radii [33]).

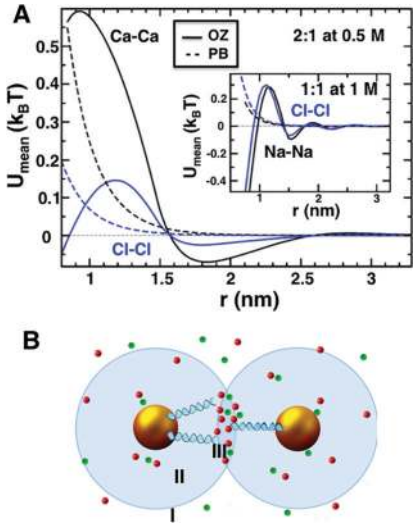

Figure 46.4 Origin of like-charge attraction at high salt concentration. (A) Calculations of the potentials of mean force in primitive model 2:1 and 1:1 electrolytes. At sufficient concentrations, like charges attract. Mean field theory [Poisson–Boltzmann (PB)] misses these attractions, while liquid-state theory [Ornstein–Zernike equation (OZ)] captures these effects. (B) Schematic of the regions that are influenced by a DNA coated AuNP (region II), and the overlap of spheres of influence of two DNA coated AuNPs (region III).

To extend these conclusions, we calculate the electrolyte-induced interaction between two smooth, parallel, like-charged surfaces, by solving the Ornstein–Zernike equation with the anisotropic hypernetted chain (HNC) closure [19, 34, 35]. The mean potential between two highly charged surfaces exhibits a qualitatively similar spatial profile as the interaction between electrolyte ions. The induced attraction is strongly amplified by a small dielectric contrast between

the surfaces and the solvent, driven by an enhanced depletion of ions caused by polarization charge. Furthermore, at small interplate separations and for high salt concentrations, exclusion of electrolyte ions from the volume confined by the two plates results in very strong interplate attraction due to the osmotic pressure difference. A similar effect for DNA-coated AuNPs could explain the crystal to glass transition observed at high salt concentrations.

DNA-coated AuNPs should attract in high salt concentrations in a manner analogous to the like-charged ions in primitive model electrolytes and the like-charged surfaces, with differences in the magnitude because of geometric reasons. Additionally, the cohesive forces driven by ion-bridging and ionic correlations are dominant in polyelectrolyte gels and blends if the pair correlation functions and the ionic-interaction potentials of the local salt are oscillatory [36], such as those shown in Fig. 46.4A. Although the mean attraction per charge can be small compared to the thermal energy (Fig. 46.4A), the attractive force between DNA-coated AuNPs should be amplified due to the polyvalency of the nanoparticles and the large number of associated ions in the overlap region of influence between two nanoparticles (region III, Fig. 46.4B). Our MD simulations point to such enhanced correlations between the DNA charges and the electrolyte-ions and between the electrolyte-ions in the DNA corona (regions II and III, Fig. 46.4B). Specifically, in going from μ_s = 15 mM to μ_s = 150 mM for a 2:1 electrolyte, the number of cations in the DNA corona increases by 25%, overcompensating the charge on DNA-coated AuNPs by ~20%. A near electroneutrality condition is achieved by a simultaneous ~12-fold increase in the number of associated anions. Second, the enhanced local concentration of cations and anions in the overlap region (region III, Fig. 46.4B) elevates the local activity of the ions, and reduces the excluded volume for the salt. This should induce depletion attractions between nanoparticles due to a locally decreased osmotic pressure. The combined effect of these cohesive forces and depletion-like attractions is calculated by the MD. Interestingly, the total effective potential as in the case of the Asakura–Oosawa depletion potential [37], is determined by the number of mediating particles (polymers in Asakura–Oosawa case; ions in the current case) in the overlap volume of the influence spheres. For the typical parameters of DNA-grafted nanoparticles in NaCl and $CaCl_2$ solutions, the effective potential may exceed $1k_BT$ if

the concentrations are, roughly, larger than 0.1 M. On the basis of these rough estimates we expect an attractive interaction between DNA-grafted nanoparticles, induced by the ions, via ion entropy, "ion bridges," and ionic cohesion. In principle, these contributions can be extracted from an algebraic form for the thermally averaged potential between two nanoparticles,

$$\frac{U_{\text{mean}}(|\mathbf{R}_1 - \mathbf{R}_2|)}{k_B T} = -V_0(|\mathbf{R}_1 - \mathbf{R}_2|) \sum_{i\varepsilon\{+,-\}} z_i (Z_{\text{I}} + Z_{\text{III}} - 2Z_{\text{II}}) \tag{46.1}$$

where V_0 is the overlap volume of region III,

$$V_0(r) = \frac{\pi}{6} D^3 \left(1 - \frac{3r}{2D} + \frac{r^3}{2D^3} \right) \tag{46.2}$$

The subindices I, II, and III refer to the regions shown in Fig. 46.4B, Z_i is an ion partition sum corresponding to region i at a fixed configuration of the nanoparticles, and z_i is the fugacity of species i. For a mixture of hard spheres and small depletants, Eq. 46.1 reduces to the Asakura–Oosawa potential, with D being the sum of the hard sphere and the depletant diameters. Ions however interact over long distance and add energetic contributions, which can be quantified by an excess chemical potential (ion cohesion), a local Donnan potential (a mean electrostatic potential), and a direct ion–nanoparticle interaction (ion bridges).

The linear dependence of the interparticle attraction on the overlap volume V_0 (Eq. 46.1) was used to obtain the size-corrected value for the MD simulations derived interparticle potential energy. Here, the radius of the influence sphere was assumed to be 2 nm greater than that for the DNA-coated AuNP to correspond to the 4 nm range of the attractive interactions. Furthermore, the interparticle attraction also increases exponentially with the counterion valency due to the Boltzmann weight in the partition sums Z_i. This correlates well with the SAXS observation that the threshold ionic strength for nanoparticle aggregation is ~5× lower for dsDNA-AuNP in $CaCl_2$ than in NaCl solutions. While the effective potential is generally attractive, the nanoparticles are stabilized by the opposing steric and electrostatic repulsions between the DNA chains, which increase sharply if the nanoparticles interdigitate.

46.3 Conclusions

We experimentally show that, in the absence of specific short-range interactions, highly charged nanoparticles undergo "gas-like" to crystalline to "glass-like" transformations with increasing salt concentration. MD simulations reveal that crystallization of the highly charged nanoparticles is driven by electrolyte-mediated attraction with a spatial extension of 4 nm from the nanoparticle surface. MD simulations and liquid-state theory suggest that the attractive interactions arise due to enhanced ionic correlations in the concentrated electrolyte and are the sum of cohesive forces and depletion interactions. These results provide fundamental insights into the very commonly observed "salting-out" phenomenon, which is extensively used to crystallize and concentrate colloids, including polyelectrolytes and proteins.

Acknowledgments

S.K., C.A.M., and M.J.B. were funded by AFOSR (FA9550-11-1-0275), L.M.M. was funded by National Defense Science and Engineering Graduate (NDSEG) fellowship, and G.I.G.-G., M.O.d.l.C., and J.W.Z. were funded by Center for Bioinspired Energy Sciences (CBES), which is an Energy Frontier Research Center funded by U.S. Department of Energy, Office of Basic Energy Sciences under Award Number DE-SC0000989. The SAXS experiments were performed at the APS 5ID-D beamline, which is supported through E. I. duPont de Nemours & Co., Northwestern University (NU), The Dow Chemical Co., and the NSF funded MRSEC at NU. The NSF-MRSEC (DMR-1121262) supported the use of J. B. Cohen X-ray diffraction facility at NU. Use of the APS was supported by DOE-BES (DE-AC02-06CH11357). We thank Steven Weigand of DND-CAT for assistance with the SAXS setup and data reduction, and Kurinji Krishnamoorthy at NU for assistance with AuNP functionalization.

References

1. Pusey, P. N. and Vanmegen, W. (1986). *Nature*, **320**, 340–342.
2. Sirota, E. B., Ouyang, H. D., Sinha, S. K., Chaikin, P. M., Axe, J. D. and Fujii, Y. (1989). *Phys. Rev. Lett.*, **62**, 1524–1527.

3. Leunissen, M. E., Christova, C. G., Hynninen, A. P., Royall, C. P., Campbell, A. I., Imhof, A., Dijkstra, M., van Roij, R. and van Blaaderen, A. (2005). *Nature*, **437**, 235–240.
4. Yethiraj, A. and van Blaaderen, A. (2003). *Nature*, **421**, 513–517.
5. Lu, P. J., Zaccarelli, E., Ciulla, F., Schofield, A. B., Sciortino, F. and Weitz, D. A. (2008). *Nature*, **453**, 499–504.
6. Mirkin, C. A., Letsinger, R. L., Mucic, R. C. and Storhoff, J. J. (1996). *Nature*, **382**, 607–609.
7. McPherson, A. (2004). *Methods*, **34**, 254–265.
8. Sacanna, S., Irvine, W. T. M., Chaikin, P. M. and Pine, D. J. (2010). *Nature*, **464**, 575–578.
9. Young, K. L., Jones, M. R., Zhang, J., Macfarlane, R. J., Esquivel-Sirvent, R., Nap, R. J., Wu, J., Schatz, G. C., Lee, B. and Mirkin, C. A. (2012). *Proc. Natl. Acad. Sci. U.S.A.*, **109**, 2240–2245.
10. Dumetz, A. C., Snellinger-O'Brien, A. M., Kaler, E. W. and Lenhoff, A. M. (2007). *Protein Sci.*, **16**, 1867–1877.
11. Rosenbaum, D., Zamora, P. C. and Zukoski, C. F. (1996). *Phys. Rev. Lett.*, **76**, 150–153.
12. Larsen, A. E. and Grier, D. G. (1997). *Nature*, **385**, 230–233.
13. Bowen, W. R. and Sharif, A. O. (1998). *Nature*, **393**, 663–665.
14. Squires, T. M. and Brenner, M. P. (2000). *Phys. Rev. Lett.*, **85**, 4976–4979.
15. Behrens, S. H. and Grier, D. G. (2001). *Phys. Rev. E: Stat. Phys. Plasmas Fluids Relat. Interdiscip. Top.*, **64**, 050401.
16. Nykypanchuk, D., Maye, M. M., van der Lelie, D. and Gang, O. (2008). *Nature*, **451**, 549–552.
17. Park, S. Y., Lytton-Jean, A. K. R., Lee, B., Weigand, S., Schatz, G. C. and Mirkin, C. A. (2008). *Nature*, **451**, 553–556.
18. Verwey, E. J. W. and Overbeek, J. T. G. (1948). *Theory of the Stability of Lyophobic Colloids* (Elsevier, New York).
19. Zwanikken, J. W. and Olvera de la Cruz, M. (2013). *Proc. Natl. Acad. Sci. U.S.A.*, **110**, 5301–5308.
20. Raspaud, E., Olvera de la Cruz, M., Sikorav, J. L. and Livolant, F. (1998). *Biophys. J.*, **74**, 381–393.
21. Wong, G. C. L. and Pollack, L. (2010). *Annu. Rev. Phys. Chem.*, **61**, 171–189.

22. Rouzina, I. and Bloomfield, V. A. (1996). *J. Phys. Chem.*, **100**, 9977–9989.
23. Tan, S. J., Kahn, J. S., Derrien, T. L., Campolongo, M. J., Zhao, M., Smilgies, D.-M. and Luo, D. (2014). *Angew. Chem. Int. Ed.*, **53**, 1316–1319.
24. Kewalramani, S., Zwanikken, J. W., Macfarlane, R. J., Leung, C. Y., Olvera de la Cruz, M., Mirkin, C. A. and Bedzyk, M. J. (2013). *ACS Nano*, **7**, 11301–11309.
25. Als-Nielsen, J. and McMorrow, D. (2011). *Elements of Modern X-Ray Physics*, 2nd ed. (John Wiley, Chichester, U.K).
26. Forster, S., Timmann, A., Konrad, M., Schellbach, C., Meyer, A., Funari, S. S., Mulvaney, P. and Knott, R. (2005). *J. Phys. Chem. B*, **109**, 1347–1360.
27. Paloli, D., Mohanty, P. S., Crassous, J. J., Zaccarelli, E. and Schurtenberger, P. (2013). *Soft Matter*, **9**, 3000–3004.
28. Finney, J. L. (1970). *Proc. R. Soc. London, Ser. A*, **319**, 479–493.
29. Hill, H. D., Macfarlane, R. J., Senesi, A. J., Lee, B., Park, S. Y. and Mirkin, C. A. (2008). *Nano Lett.*, **8**, 2341– 2344.
30. Qiu, X. Y., Kwok, L. W., Park, H. Y., Lamb, J. S., Andresen, K. and Pollack, L. (2006). *Phys. Rev. Lett.*, **96**, 138101.
31. Koltover, I., Wagner, K. and Safinya, C. R. (2000). *Proc. Natl. Acad. Sci. U.S.A.*, **97**, 14046.
32. Truzzolillo, D., Bordi, F., Sciortino, F. and Sennato, S. (2010). *J. Chem. Phys.*, **133**, 024901.
33. Nightingale, E. R. (1959). *J. Phys. Chem.*, **63**, 1381–1387.
34. Jing, Y. F., Jadhao, V., Zwanikken, J. W. and Olvera de la Cruz, M. (2015). *J. Chem. Phys.*, **143**, 194508.
35. Kjellander, R. and Marcelja, S. (1984). *Chem. Phys. Lett.*, **112**, 49–53.
36. Sing, C. E., Zwanikken, J. W. and Olvera de la Cruz, M. (2014). *Nat. Mater.*, **13**, 694–698.
37. Asakura, S. and Oosawa, F. (1958). *J. Polym. Sci.*, **33**, 183–192.